

Majorana Kramers pairs in higher-order topological insulators

Chen-Hsuan Hsu¹, Peter Stano^{1,2,3}, Jelena Klinovaja^{1,4}, and Daniel Loss^{1,4}

¹*RIKEN Center for Emergent Matter Science (CEMS), Wako, Saitama 351-0198, Japan*

²*Department of Applied Physics, School of Engineering,*

University of Tokyo, 7-3-1 Hongo, Bunkyo-ku, Tokyo 113-8656, Japan

³*Institute of Physics, Slovak Academy of Sciences, 845 11 Bratislava, Slovakia and*

⁴*Department of Physics, University of Basel, Klingelbergstrasse 82, CH-4056 Basel, Switzerland*

(Dated: November 8, 2018)

We propose a tune-free scheme to realize Kramers pairs of Majorana bound states in recently discovered higher-order topological insulators (HOTIs). We show that, by bringing two hinges of a HOTI into the proximity of an s -wave superconductor, the competition between local and crossed Andreev pairing leads to the formation of Majorana Kramers pairs, when the latter pairing dominates over the former. We demonstrate that such a topological superconductivity is stabilized by moderate electron-electron interactions. The proposed setup avoids the application of a magnetic field or local voltage gates, and requires weaker interactions compared with nonhelical nanowires.

Majorana bound states (MBSs), with topological quantum computation prospects, have gained much attention recently [1–31]. However, the prototypical realizations based on proximity-induced superconductivity and either semiconducting nanowires with strong spin-orbit interactions [32–44], or topological insulators (TIs) [45, 46] require an external magnetic field, detrimental to superconductivity and MBSs themselves. It might also be noted that buried Dirac points are common in two-/three-dimensional TIs (2DTIs/3DTIs) [47–51], impeding the realization of MBSs in TI-superconductor heterostructures using magnetic fields [47].

Platforms without magnetic fields are therefore searched for [52–58], examples including helical spin textures [59–66] and crossed Andreev pairings in double nanowires or 2DTI edge channels [67–73]. In the former, the spin texture arises through indirect coupling mediated by itinerant carriers. The superconducting gap reduces it, leading to a tradeoff between the operation temperature (set by the indirect coupling) and the MBS localization length (set by the superconducting gap). On the other hand, the latter setup requires fine-tuned chemical potentials in two isolated one-dimensional channels. These difficulties motivate us to seek a new scheme to avoid fine-tuning.

Here we propose such a scheme, exploiting the recently discovered higher-order topological insulators (HOTIs) [74–82]. Specifically, we focus on 3D helical second-order TIs. In contrast to the gapless surface states in their first-order counterparts [6, 7, 83–86], these HOTIs host helical hinge states, in which opposite spins move in opposite directions, akin to the spin-momentum locked edge channels in 2DTIs [87–93]. Important for us, these hinges form one-dimensional channels of identical chemical potentials. There is compelling experimental evidence for the topological hinge states in Bi(111) nanowires and bilayers [80, 94, 95].

Our scheme exploits s -wave superconductivity-proximitized helical hinges of a HOTI. Two types of pairings arise, a local (standard) and a nonlocal (crossed Andreev) one. We first demonstrate that Majorana Kramers pairs (MKPs) emerge when the crossed Andreev pairing

dominates. This regime, however, does not arise in a non-interacting system. Nevertheless, we show that rather weak electron-electron interactions are sufficient to push the system into a regime where the crossed Andreev pairing dominates. We therefore predict that MKPs typically appear at the ends of a HOTI nanowire.

To elucidate an essential feature, consider that two parallel hinges of a helical HOTI are in contact with an s -wave superconductor. Cooper pairs can tunnel into the hinges through two processes. The local (nonlocal) pairing process corresponds to the two partners of a Cooper pair tunneling into the same (different) hinge(s). We denote the configuration as *parahelical* (*orthohelical*), when the helicities of the two hinges are *the same* (*opposite*). For example, in the parahelical setup spin-down electrons in the two hinges propagate in the same direction, whereas in the orthohelical setup they move in opposite directions. The momentum conservation imposes selection rules: the chemical potentials of the two hinges have to be the same (opposite) for the parahelical (orthohelical) setup [68] to allow for a crossed Andreev pairing. Since the conducting hinges of a HOTI are all connected, their chemical potentials are identical *without applying local voltage gates*, a substantial advantage.

Setup. As a concrete example, we consider the recently discovered HOTI material, a bismuth crystal grown along the (111) axis,¹ which hosts helical hinge states [80], as drawn in Fig. 1. Since the helicities of any two parallel hinges on the same lateral facet are opposite, the orthohelical setup is realized when a superconductor covers one lateral facet with two parallel hinges. In this case, crossed Andreev pairing is not feasible.

However, when the superconductor extends over two lateral facets (see the right panel of Fig. 1), it is in contact with three

¹ Even though bismuth is a bulk semimetal, the topologically trivial bulk states can be gapped by, e.g., superconductivity, disorder or finite-size effects [80, 82, 91, 93, 95]. Further, while we take Bi(111) nanowires as an example, our setup can be implemented also in other recently predicted helical HOTI materials, such as SnTe, Bi₂TeI, BiSe, and BiTe [76].

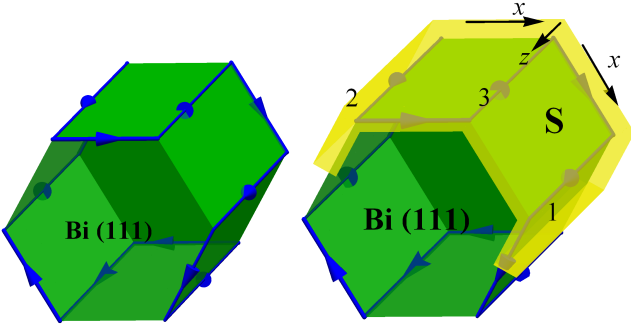


FIG. 1. Left: In a Bi(111) nanowire (green), the gapless states (blue arrows) propagate along the hinges. The spin-up (-down) hinge states move against (along) the directions of the arrows. The helicities of any two parallel hinge states [along $z \equiv (111)$ axis] on a single lateral facet are opposite. Right: In the proposed setup, a superconducting layer (yellow) covers three parallel hinges (labeled by 1, 2, and 3). The (1,2) pair carries the same helicity, allowing for the crossed Andreev pairing. For other pairs, [(1,3) and (2,3)], such pairing is suppressed. The x axis of the local coordinate is defined along the perimeter of the hexagonal cross section, and the y axis (not shown) is normal to the lateral facets.

parallel hinges along $z \equiv (111)$ axis. Two of them (labeled by 1 and 2) carry the same helicity while the third one (labeled by 3) the opposite. The momentum selection rules, together with uniform chemical potential (assumed to be in the bulk gap and not very close to the Dirac point) allow a crossed Andreev pairing between the hinges 1 and 2 and forbid it between the orthohelical hinges [(1,3) and (2,3) pairs], see Fig. 2. As a result, the hinge 3 decouples from the remaining two and the parahalical setup is realized in the hinges 1 and 2 [96].

Model. From now on we restrict ourselves to the two coupled hinges.² We model them using the fields

$$\psi_n(r) = R_{n,\downarrow}(r)e^{ik_F r} + L_{n,\uparrow}(r)e^{-ik_F r}, \quad (1)$$

with the coordinate r along the hinge, the hinge index $n \in \{1, 2\}$, the Fermi wave number k_F , and the slowly varying right- and left-moving fields $R_{n,\downarrow}$ and $L_{n,\uparrow}$, respectively. Whenever possible, we suppress the coordinate r and the spin index, the latter fixed by the spin-momentum locking. In a noninteracting system, the effective Hamiltonian reads $H = H_0 + H_{\text{intra}} + H_c$. The kinetic energy term is

$$H_0 = -i\hbar v_F \sum_{n=1,2} \int dr \left(R_n^\dagger \partial_r R_n - L_n^\dagger \partial_r L_n \right), \quad (2)$$

with the Fermi velocity v_F . The local pairing term is

$$H_{\text{intra}} = \sum_{n=1,2} \int dr \left[\frac{\Delta_n}{2} (R_n^\dagger L_n^\dagger - L_n^\dagger R_n^\dagger) + \text{H.c.} \right], \quad (3)$$

² We consider a clean system with identical Fermi wave numbers for the two identical hinges. However, our results are robust against weak disorder [96].

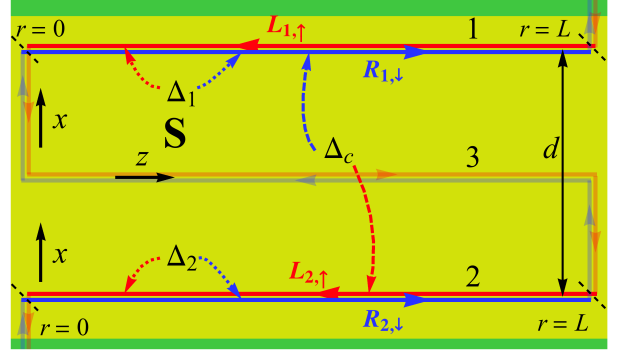


FIG. 2. Schematics of the parahalical setup in the xz plane of the local coordinate (view from the $+y$ direction) with the hinge coordinate r . A superconductor (yellow) covers three long hinges (along the z direction), and several short hinges (along the x direction). In hinges 1 and 2, which are at distance d , the spin-up states propagate toward the $-r$ direction (red solid arrows) while the spin-down states toward $+r$ (blue solid arrows). Hinge 3 is decoupled from the others. The local ($\Delta_{1,2}$) and crossed Andreev (Δ_c) pairing processes are indicated by the dotted and dashed arrows, respectively. Since the short segments along the x direction are not aligned in the laboratory frame, Δ_c is suppressed if $r \notin [0, L]$, while $\Delta_{1,2}$ remains constant for any r , including in the short segments. As a result, the boundaries (black dashed lines) are created at $r = 0$ and $r = L$ (the ends of the nanowire), which are assumed to be far apart on the scale of the Majorana localization length. For clarity, only one crossed Andreev pairing process, $\Delta_c R_{1,\downarrow}^\dagger L_{2,\uparrow}^\dagger$, is depicted.

with the pairing gap Δ_n in the hinge n . Finally, the crossed Andreev pairing term is

$$H_c = \int dr \left[\frac{\Delta_c}{2} (R_1^\dagger L_2^\dagger - L_2^\dagger R_1^\dagger) + (1 \leftrightarrow 2) \right] + \text{H.c.}, \quad (4)$$

with the pairing gap Δ_c . For simplicity, we take a spatially uniform real local pairing gap $\Delta_n > 0$. On the other hand, the crossed Andreev pairing gap Δ_c changes its (real) value from finite ($r \in [0, L]$) to zero ($r \notin [0, L]$), creating two boundaries at $r = 0$ and $r = L$, as indicated in Fig. 2. Assuming the hinge length L being sufficiently long, we focus only on the boundary at $r = 0$ and demonstrate the existence of a MKP localized there.

Majorana Kramers pairs. We first identify the criterion for MKPs in a noninteracting system. The single-particle Hamiltonian, see Eqs. (2)–(4), can be written in the basis $\Psi = (R_1, L_1, R_2, L_2, R_1^\dagger, L_1^\dagger, R_2^\dagger, L_2^\dagger)^T$ as $H = \frac{1}{2} \int dr \Psi^\dagger(r) \mathcal{H}(r) \Psi(r)$, with the Hamiltonian density

$$\begin{aligned} \mathcal{H}(r) = & -i\hbar v_F \eta^0 \tau^0 \sigma^z \partial_r - \Delta_+ \eta^y \tau^0 \sigma^y \\ & - \Delta_- \eta^y \tau^z \sigma^y - \Delta_c \eta^y \tau^x \sigma^y, \end{aligned} \quad (5)$$

with $\Delta_\pm = (\Delta_1 \pm \Delta_2)/2$. In the above, the matrices η^μ , τ^μ , and σ^μ act on the particle-hole, hinge, and spin space, respectively. They are given by the Pauli (identity) matrix for $\mu = x, y, z$ ($\mu = 0$). The bulk spectrum is two-fold degenerate due to the time-reversal symmetry (TRS), with a gap

denoted as Δ_b . The reversal of the sign of Δ_b , which can be shown to coincide with the sign of $(\Delta_1\Delta_2 - \Delta_c^2)$, indicates the band inversion and suggests the presence of zero-energy MBSs at a boundary.

By directly solving the Bogoliubov–de Gennes equation of Eq. (5) at zero energy [65, 97], one can show that such bound states are indeed present [96]. With this procedure, we find that a MKP at $r = 0$ (and another pair at $r = L$) emerges if and only if

$$\Delta_c^2 > \Delta_1\Delta_2. \quad (6)$$

Because of its topological origin, the MKP appears and disappears wherever Δ_b reverses its sign even in setups with different model details, for example, a less abrupt change of Δ_c . Similarly, additional second-order (co-)tunneling processes [68, 72, 98] not included here do not affect the topological criterion as long as the local pairing gaps Δ_n are of similar strengths [96]. We therefore conclude that the criterion for MKPs is the crossed Andreev pairing to be dominant over the local pairing, as described by Eq. (6). In noninteracting systems, however, Eq. (6) cannot be fulfilled [98]. Including electron–electron interactions is thus essential for our scheme. Below we demonstrate that even moderate interactions can drive the system into the topological superconducting phase hosting MKPs.

Interacting system. To begin, we note that since our setup respects TRS, the elastic backscattering is precluded in the helical channels (unless the TRS is broken, for example, by nuclear spins [99, 100]). We therefore include only the forward scattering processes into the interaction H_{int} and bosonize the total hinge Hamiltonian $H_{\text{el}} = H_0 + H_{\text{int}}$. This procedure leads to two copies of the helical Tomonaga-Luttinger liquid,

$$H_{\text{el}} = \sum_{n=1,2} \int \frac{\hbar dr}{2\pi} \left\{ u_n K_n [\partial_r \theta_n(r)]^2 + \frac{u_n}{K_n} [\partial_r \phi_n(r)]^2 \right\}, \quad (7)$$

with the interaction parameter K_n for the hinge n and the modified velocity $u_n = v_F/K_n$. Using standard bosonic fields θ_n and ϕ_n for helical channels [99, 100], the local pairing term reads

$$H_{\text{intra}} = \sum_{n=1,2} \frac{\Delta_n}{\pi a} \int dr \cos[2\theta_n(r)], \quad (8)$$

where a is the short-distance cutoff, taken to be the transverse decay length of the hinge states. The crossed Andreev pairing term is

$$H_c = \frac{2\Delta_c}{\pi a} \int dr \cos[\theta_1(r) + \theta_2(r)] \cos[\phi_1(r) - \phi_2(r)]. \quad (9)$$

Above certain interaction strength, the crossed Andreev pairing dominates and the topological criterion [see Eq. (6)] is satisfied. To show this, we derive the renormalization-group

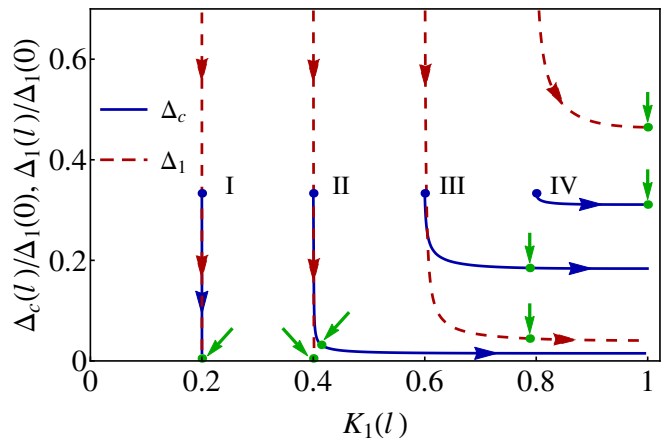


FIG. 3. RG flow diagram. We take the parameters $K_1(0) = K_2(0) = 0.2, 0.4, 0.6,$ and 0.8 , $\tilde{\Delta}_1(0) = \tilde{\Delta}_2(0) = 3\tilde{\Delta}_c(0) = 0.03$, $a(0) = 5$ nm, and $L = 1$ μm . The crossed Andreev (local) pairing gap Δ_c ($\Delta_1 = \Delta_2$) is plotted in blue solid (red dashed) curves. The blue dots (labeled by I–IV) mark the initial points of Δ_c , and the green arrows and points specify where the RG flows stop. The RG flows labeled by II and III stop at the points at which the renormalized crossed Andreev pairing dominates over the local pairing ($\Delta_c > \Delta_1$), indicating topological superconducting phase.

(RG) flow equations [96] following standard procedure [101]. To simplify the analysis, we introduce the dimensionless coupling constants,

$$\tilde{\Delta}_n(l) = \frac{\Delta_n(l)a(l)}{\hbar u_n}, \quad \tilde{\Delta}_c(l) = \frac{\Delta_c(l)a(l)}{\hbar \sqrt{u_1 u_2}}, \quad (10)$$

with $l \equiv \ln[a(l)/a(0)]$. For given initial parameters (at $l = 0$), we numerically propagate the RG flow equations. We stop the RG flow whenever any of the dimensionless coupling constants becomes unity. At these points we obtain the renormalized gaps and evaluate the criterion for the MKP existence.

An example of the RG flow is in Fig. 3, showing how the pairing gaps evolve for several starting values. The repulsive interaction tends to reduce both types of the pairing. Importantly, due to the local nature of the Coulomb interaction, the suppression is stronger for the local pairing (red dashed curve) than for the crossed Andreev pairing (blue solid curve): *the repulsive interaction favors the nonlocal pairing*. Consequently, even if in their initial values the local pairing dominates over the crossed Andreev pairing [we take $\tilde{\Delta}_c(0)/\tilde{\Delta}_1(0) = 1/3$ in Fig. 3], a sufficiently strong interaction can reverse this relation.

To prove that Eq. (6) with the renormalized pairing gaps is the correct criterion, we note that the end points of the RG flows (green arrows) are adiabatically connected to the noninteracting limit without closing the bulk gap. Here, the model can be reformionized into Eq. (5) with renormalized pairing gaps [102]. The reformionized model can be used to justify the existence of MKPs and allows us to estimate their localization length. It is typically around 20 nm and much shorter than the hinge length $L \sim 1$ μm [96]. We thus conclude that

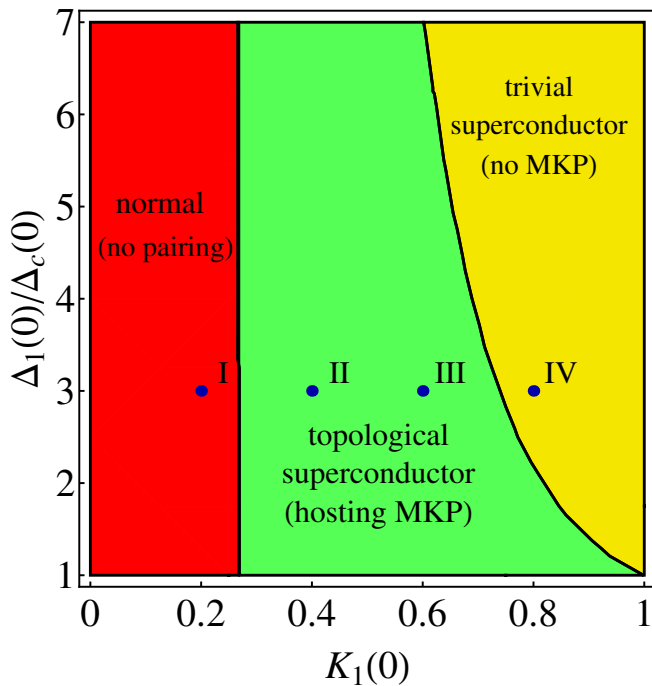


FIG. 4. Phase diagram. The vertical and horizontal axes label the initial values of the gap ratio $[\Delta_1(0)/\Delta_c(0)]$ and interaction parameter $K_1(0) = K_2(0)$, respectively. The other parameters are the same as those in Fig. 3. The green (yellow) region marks the phase with (without) MKPs. The corresponding RG flows to the blue dots (labeled by I–IV) are shown in Fig. 3. In the red region, both types of the pairing gaps vanish.

sufficiently strong electron-electron interactions can stabilize well isolated MKPs.

Phase diagram. To investigate the stability of the MKPs in the parameter space, we repeat the above numerical procedure for $K_1(0) \in [0, 1]$ and $\Delta_1(0)/\Delta_c(0) \in [1, 7]$, see Fig. 4. In the phase diagram, the green (yellow) color stands for the region in which MKPs are present (absent). If the system is non-interacting, the MKPs are absent, consistent with Ref. [98]. For $\Delta_1(0)/\Delta_c(0) \gtrsim 1$, a rather weak interaction $K_n(0) \lesssim 1$ can stabilize the MKPs. The larger $\Delta_1(0)/\Delta_c(0)$ is, the stronger interaction is required to reverse the gap strengths. A very strong interaction [red region; $K_1(0) < 2 - \sqrt{3} \approx 0.27$] destroys both types of the pairing gaps. Further, we estimate the initial values $K_1(0) \lesssim 0.6$ [103] and $\Delta_1(0)/\Delta_c(0) = O(1)$ [96], and find that they are compatible with the MKP regime in Fig. 4.

In comparison with nonhelical nanowires [73], our setup requires weaker interactions to induce MKPs. The difference between nonhelical and helical channels can be understood as follows. The effects of electron-electron interactions in nonhelical channels are “averaged” over charge and (noninteracting) spin sectors, and thus weakened as compared to helical channels. This quantitative difference indicates the advantage of helical channels, making HOTIs a promising platform for topological superconductivity without the need of magnetic

fields.

We perform the same RG analysis in the standard but more involved source-term approach [73, 104], in which one incorporates explicitly the inter-hinge separation d and coherence length ξ_s of the superconductor, instead of relying on knowing the initial values of $\Delta_1(0)$ and $\Delta_c(0)$ in the effective Hamiltonian. This analysis gives essentially the same phase diagram as in Fig. 4; see Ref. [96]. For the parameters of bismuth hinges [80, 93, 105], we find that moderate interactions can render a dominant crossed Andreev pairing for $d \sim 100$ nm and $\xi_s \sim 1$ μ m. With these quantitative examinations [96], we conclude that our setup is accessible in realistic samples.

Discussion. Our work indicates that generally MKPs can be supported at the ends of a HOTI nanowire proximity coupled to a superconductor without fine-tuning. We remark that the hinge states are known to survive even when spatial symmetries are broken by weak local perturbations due to disorder, as long as the TRS is preserved [80]. As a consequence, the MKPs proposed in this work are robust against TRS-preserving disorder. It is also worth pointing out that, in addition to the MKPs, our setup can work as a Cooper pair splitter—a source of spatially separated spin-entangled electron pairs [106–118]. Finally, we remark that detection of MKPs with the parity-controlled 2π Josephson effect, which gives distinct signatures from unpaired MBSs [119], and braiding-based [120, 121] or measurement-based [122] quantum computation schemes utilizing MKPs have been widely discussed in the literature. Compared to setups without TRS, since here the MKPs require no magnetic fields, they are protected by a larger superconducting gap, leading to shorter localization length and longer coherence time [72, 122]. Our setup provides building blocks for the measurement-based structures proposed in Refs. [123–125], which offers a route to scalable architectures for topological quantum computation.

We thank R. S. Deacon for helpful discussion. This work was supported financially by the JSPS Kakenhi Grant No. 16H02204, by the Swiss National Science Foundation (Switzerland), and by the NCCR QSIT. This project received funding from the European Unions Horizon 2020 research and innovation program (ERC Starting Grant, Grant Agreement No 757725).

-
- [1] A. Y. Kitaev, Unpaired Majorana fermions in quantum wires, *Phys. Usp.* **44**, 131 (2001).
 - [2] A. Y. Kitaev, Fault-tolerant quantum computation by anyons, *Ann. Phys.* **303**, 2 (2003).
 - [3] C. Nayak, S. H. Simon, A. Stern, M. Freedman, and S. Das Sarma, Non-Abelian anyons and topological quantum computation, *Rev. Mod. Phys.* **80**, 1083 (2008).
 - [4] Y. Tanaka, T. Yokoyama, and N. Nagaosa, Manipulation of the Majorana Fermion, Andreev Reflection, and Josephson Current on Topological Insulators, *Phys. Rev. Lett.* **103**, 107002 (2009).
 - [5] M. Sato and S. Fujimoto, Topological phases of noncentrosymmetric superconductors: Edge states, Majorana fermions, and

- non-Abelian statistics, *Phys. Rev. B* **79**, 094504 (2009).
- [6] M. Z. Hasan and C. L. Kane, *Colloquium*: Topological insulators, *Rev. Mod. Phys.* **82**, 3045 (2010).
- [7] X.-L. Qi and S.-C. Zhang, Topological insulators and superconductors, *Rev. Mod. Phys.* **83**, 1057 (2011).
- [8] J. Alicea, Y. Oreg, G. Refael, F. von Oppen, and M. P. A. Fisher, Non-Abelian statistics and topological quantum information processing in 1D wire networks, *Nat. Phys.* **7**, 412 (2011).
- [9] A. Cook and M. Franz, Majorana fermions in a topological-insulator nanowire proximity-coupled to an *s*-wave superconductor, *Phys. Rev. B* **84**, 201105 (2011).
- [10] J. Klinovaja, P. Stano, and D. Loss, Transition from fractional to Majorana fermions in Rashba nanowires, *Phys. Rev. Lett.* **109**, 236801 (2012).
- [11] D. Chevallier, D. Sticlet, P. Simon, and C. Bena, Mutation of Andreev into Majorana bound states in long superconductor-normal and superconductor-normal-superconductor junctions, *Phys. Rev. B* **85**, 235307 (2012).
- [12] F. Domínguez, F. Hassler, and G. Platero, Dynamical detection of Majorana fermions in current-biased nanowires, *Phys. Rev. B* **86**, 140503 (2012).
- [13] J. Klinovaja, S. Gangadharaiah, and D. Loss, Electric-field-induced majorana fermions in armchair carbon nanotubes, *Phys. Rev. Lett.* **108**, 196804 (2012).
- [14] Y. Niu, S. B. Chung, C.-H. Hsu, I. Mandal, S. Raghu, and S. Chakravarty, Majorana zero modes in a quantum Ising chain with longer-ranged interactions, *Phys. Rev. B* **85**, 035110 (2012).
- [15] E. Prada, P. San-Jose, and R. Aguado, Transport spectroscopy of *NS* nanowire junctions with Majorana fermions, *Phys. Rev. B* **86**, 180503 (2012).
- [16] B. M. Terhal, F. Hassler, and D. P. DiVincenzo, From Majorana fermions to topological order, *Phys. Rev. Lett.* **108**, 260504 (2012).
- [17] C. Beenakker, Search for Majorana Fermions in Superconductors, *Ann. Rev. Condens. Matter Phys.* **4**, 113 (2013).
- [18] K. Björnson and A. M. Black-Schaffer, Vortex states and Majorana fermions in spin-orbit coupled semiconductor-superconductor hybrid structures, *Phys. Rev. B* **88**, 024501 (2013).
- [19] S. Nakosai, J. C. Budich, Y. Tanaka, B. Trauzettel, and N. Nagaosa, Majorana Bound States and Nonlocal Spin Correlations in a Quantum Wire on an Unconventional Superconductor, *Phys. Rev. Lett.* **110**, 117002 (2013).
- [20] M. Thakurathi, A. A. Patel, D. Sen, and A. Dutta, Floquet generation of Majorana end modes and topological invariants, *Phys. Rev. B* **88**, 155133 (2013).
- [21] E. Dumitrescu, J. D. Sau, and S. Tewari, Magnetic field response and chiral symmetry of time-reversal-invariant topological superconductors, *Phys. Rev. B* **90**, 245438 (2014).
- [22] F. Maier, J. Klinovaja, and D. Loss, Majorana fermions in Ge/Si hole nanowires, *Phys. Rev. B* **90**, 195421 (2014).
- [23] L. Weithofer, P. Recher, and T. L. Schmidt, Electron transport in multiterminal networks of Majorana bound states, *Phys. Rev. B* **90**, 205416 (2014).
- [24] R. S. Deacon, J. Wiedenmann, E. Bocquillon, F. Domínguez, T. M. Klapwijk, P. Leubner, C. Brüne, E. M. Hankiewicz, S. Tarucha, K. Ishibashi, H. Buhmann, and L. W. Molenkamp, Josephson radiation from gapless Andreev bound states in HgTe-based topological junctions, *Phys. Rev. X* **7**, 021011 (2017).
- [25] G.-Y. Huang and H. Q. Xu, Majorana fermions in topological-insulator nanowires: From single superconducting nanowires to Josephson junctions, *Phys. Rev. B* **95**, 155420 (2017).
- [26] W. Izumida, L. Milz, M. Marganska, and M. Grifoni, Topology and zero energy edge states in carbon nanotubes with superconducting pairing, *Phys. Rev. B* **96**, 125414 (2017).
- [27] J. Manousakis, A. Altland, D. Bagrets, R. Egger, and Y. Ando, Majorana qubits in a topological insulator nanoribbon architecture, *Phys. Rev. B* **95**, 165424 (2017).
- [28] A. Ptok, A. Kobińska, and T. Domański, Controlling the bound states in a quantum-dot hybrid nanowire, *Phys. Rev. B* **96**, 195430 (2017).
- [29] M. Sato and Y. Ando, Topological superconductors: a review, *Rep. Prog. Phys.* **80**, 076501 (2017).
- [30] C. Reeg, D. Loss, and J. Klinovaja, Proximity effect in a two-dimensional electron gas coupled to a thin superconducting layer, *Beilstein J. Nanotechnol.* **9**, 1263 (2018).
- [31] M. Trif, O. Dmytruk, H. Bouchiat, R. Aguado, and P. Simon, Dynamic current susceptibility as a probe of Majorana bound states in nanowire-based Josephson junctions, *Phys. Rev. B* **97**, 041415 (2018).
- [32] R. M. Lutchyn, J. D. Sau, and S. Das Sarma, Majorana Fermions and a Topological Phase Transition in Semiconductor-Superconductor Heterostructures, *Phys. Rev. Lett.* **105**, 077001 (2010).
- [33] Y. Oreg, G. Refael, and F. von Oppen, Helical Liquids and Majorana Bound States in Quantum Wires, *Phys. Rev. Lett.* **105**, 177002 (2010).
- [34] V. Mourik, K. Zuo, S. M. Frolov, S. R. Plissard, E. P. A. M. Bakkers, and L. P. Kouwenhoven, Signatures of Majorana Fermions in Hybrid Superconductor-Semiconductor Nanowire Devices, *Science* **336**, 1003 (2012).
- [35] A. Das, Y. Ronen, Y. Most, Y. Oreg, M. Heiblum, and H. Shtrikman, Zero-bias peaks and splitting in an InAs nanowire topological superconductor as a signature of Majorana fermions, *Nat. Phys.* **8**, 887 (2012).
- [36] M. T. Deng, C. L. Yu, G. Y. Huang, M. Larsson, P. Caroff, and H. Q. Xu, Anomalous Zero-Bias Conductance Peak in a Nb-InSb Nanowire-Nb Hybrid Device, *Nano Lett.* **12**, 6414 (2012).
- [37] L. P. Rokhinson, X. Liu, and J. K. Furdyna, The fractional a.c. Josephson effect in a semiconductor-superconductor nanowire as a signature of Majorana particles, *Nat. Phys.* **8**, 795 (2012).
- [38] A. D. K. Finck, D. J. Van Harlingen, P. K. Mohseni, K. Jung, and X. Li, Anomalous Modulation of a Zero-Bias Peak in a Hybrid Nanowire-Superconductor Device, *Phys. Rev. Lett.* **110**, 126406 (2013).
- [39] H. O. H. Churchill, V. Fatemi, K. Grove-Rasmussen, M. T. Deng, P. Caroff, H. Q. Xu, and C. M. Marcus, Superconductor-nanowire devices from tunneling to the multichannel regime: Zero-bias oscillations and magnetoconductance crossover, *Phys. Rev. B* **87**, 241401 (2013).
- [40] D. Rainis, L. Trifunovic, J. Klinovaja, and D. Loss, Towards a realistic transport modeling in a superconducting nanowire with Majorana fermions, *Phys. Rev. B* **87**, 024515 (2013).
- [41] S. Takei, B. M. Fregoso, H.-Y. Hui, A. M. Lobos, and S. Das Sarma, Soft Superconducting Gap in Semiconductor Majorana Nanowires, *Phys. Rev. Lett.* **110**, 186803 (2013).
- [42] S. M. Albrecht, A. P. Higginbotham, M. Madsen, F. Kuemmeth, T. S. Jespersen, J. Nygård, P. Krogstrup, and C. M. Marcus, Exponential protection of zero modes in Majorana islands, *Nature* **531**, 206 (2016).
- [43] O. Gül, H. Zhang, J. D. S. Bommer, M. W. A. de Moor, D. Car, S. R. Plissard, E. P. A. M. Bakkers, A. Geresdi, K. Watanabe, T. Taniguchi, and L. P. Kouwenhoven, Ballistic Majorana nanowire devices, *Nat. Nanotech.* **13**, 192 (2018).
- [44] H. Zhang, C.-X. Liu, S. Gazibegovic, D. Xu, J. A. Logan,

- G. Wang, N. van Loo, J. D. S. Bommer, M. W. A. de Moor, D. Car, R. L. M. O. het Veld, P. J. van Veldhoven, S. Koelling, M. A. Verheijen, M. Pendharkar, D. J. Pennachio, B. Shojaei, J. S. Lee, C. J. Palmström, E. P. A. M. Bakkers, S. D. Sarma, and L. P. Kouwenhoven, Quantized Majorana conductance, *Nature* **556**, 74 (2018).
- [45] L. Fu and C. L. Kane, Superconducting Proximity Effect and Majorana Fermions at the Surface of a Topological Insulator, *Phys. Rev. Lett.* **100**, 096407 (2008).
- [46] L. Fu and C. L. Kane, Josephson current and noise at a superconductor/quantum-spin-Hall-insulator/superconductor junction, *Phys. Rev. B* **79**, 161408 (2009).
- [47] R. Skolasinski, D. I. Pikulin, J. Alicea, and M. Wimmer, Robust Helical Edge Transport in Quantum Spin Hall Quantum Wells, ArXiv e-prints (2017), arXiv:1709.04830 [cond-mat.mes-hall].
- [48] H. Zhang, C.-X. Liu, X.-L. Qi, X. Dai, Z. Fang, and S.-C. Zhang, Topological insulators in Bi_2Se_3 , Bi_2Te_3 and Sb_2Te_3 with a single Dirac cone on the surface, *Nat. Phys.* **5**, 438 (2009).
- [49] D. Hsieh, Y. Xia, D. Qian, L. Wray, F. Meier, J. H. Dil, J. Osterwalder, L. Patthey, A. V. Fedorov, H. Lin, A. Bansil, D. Grauer, Y. S. Hor, R. J. Cava, and M. Z. Hasan, Observation of Time-Reversal-Protected Single-Dirac-Cone Topological-Insulator States in Bi_2Te_3 and Sb_2Te_3 , *Phys. Rev. Lett.* **103**, 146401 (2009).
- [50] C. Brüne, C. X. Liu, E. G. Novik, E. M. Hankiewicz, H. Buhmann, Y. L. Chen, X. L. Qi, Z. X. Shen, S. C. Zhang, and L. W. Molenkamp, Quantum Hall Effect from the Topological Surface States of Strained Bulk HgTe, *Phys. Rev. Lett.* **106**, 126803 (2011).
- [51] C.-A. Li, S.-B. Zhang, and S.-Q. Shen, Hidden edge Dirac point and robust quantum edge transport in InAs/GaSb quantum wells, *Phys. Rev. B* **97**, 045420 (2018).
- [52] A. Keselman, L. Fu, A. Stern, and E. Berg, Inducing Time-Reversal-Invariant Topological Superconductivity and Fermion Parity Pumping in Quantum Wires, *Phys. Rev. Lett.* **111**, 116402 (2013).
- [53] A. Haim, A. Keselman, E. Berg, and Y. Oreg, Time-reversal-invariant topological superconductivity induced by repulsive interactions in quantum wires, *Phys. Rev. B* **89**, 220504 (2014).
- [54] C. Schrade, A. A. Zyuzin, J. Klinovaja, and D. Loss, Proximity-Induced π Josephson Junctions in Topological Insulators and Kramers Pairs of Majorana Fermions, *Phys. Rev. Lett.* **115**, 237001 (2015).
- [55] C. L. M. Wong and K. T. Law, Majorana Kramers doublets in $d_{x^2-y^2}$ -wave superconductors with Rashba spin-orbit coupling, *Phys. Rev. B* **86**, 184516 (2012).
- [56] F. Zhang, C. L. Kane, and E. J. Mele, Time-Reversal-Invariant Topological Superconductivity and Majorana Kramers Pairs, *Phys. Rev. Lett.* **111**, 056402 (2013).
- [57] S. Hoffman, J. Klinovaja, and D. Loss, Topological phases of inhomogeneous superconductivity, *Phys. Rev. B* **93**, 165418 (2016).
- [58] Z. Yan, F. Song, and Z. Wang, Majorana Corner Modes in a High-Temperature Platform, *Phys. Rev. Lett.* **121**, 096803 (2018).
- [59] J. Klinovaja, P. Stano, A. Yazdani, and D. Loss, Topological superconductivity and Majorana fermions in RKKY systems, *Phys. Rev. Lett.* **111**, 186805 (2013).
- [60] B. Braunecker and P. Simon, Interplay between Classical Magnetic Moments and Superconductivity in Quantum One-Dimensional Conductors: Toward a Self-Sustained Topological Majorana Phase, *Phys. Rev. Lett.* **111**, 147202 (2013).
- [61] M. M. Vazifeh and M. Franz, Self-Organized Topological State with Majorana Fermions, *Phys. Rev. Lett.* **111**, 206802 (2013).
- [62] S. Nadj-Perge, I. K. Drozdov, B. A. Bernevig, and A. Yazdani, Proposal for realizing Majorana fermions in chains of magnetic atoms on a superconductor, *Phys. Rev. B* **88**, 020407 (2013).
- [63] S. Nadj-Perge, I. K. Drozdov, J. Li, H. Chen, S. Jeon, J. Seo, A. H. MacDonald, B. A. Bernevig, and A. Yazdani, Observation of Majorana fermions in ferromagnetic atomic chains on a superconductor, *Science* **346**, 602 (2014).
- [64] F. Pientka, L. I. Glazman, and F. von Oppen, Unconventional topological phase transitions in helical Shiba chains, *Phys. Rev. B* **89**, 180505 (2014).
- [65] C.-H. Hsu, P. Stano, J. Klinovaja, and D. Loss, Antiferromagnetic nuclear spin helix and topological superconductivity in ^{13}C nanotubes, *Phys. Rev. B* **92**, 235435 (2015).
- [66] R. Pawlak, M. Kisiel, J. Klinovaja, T. Meier, S. Kawai, T. Glatzel, D. Loss, and E. Meyer, Probing atomic structure and Majorana wavefunctions in monoatomic Fe chains on superconducting Pb surface, *npj Quantum Information* **2**, 16035 (2016).
- [67] E. Gaidamauskas, J. Paaske, and K. Flensberg, Majorana Bound States in Two-Channel Time-Reversal-Symmetric Nanowire Systems, *Phys. Rev. Lett.* **112**, 126402 (2014).
- [68] J. Klinovaja, A. Yacoby, and D. Loss, Kramers pairs of Majorana fermions and parafermions in fractional topological insulators, *Phys. Rev. B* **90**, 155447 (2014).
- [69] J. Klinovaja and D. Loss, Time-reversal invariant parafermions in interacting Rashba nanowires, *Phys. Rev. B* **90**, 045118 (2014).
- [70] J. Klinovaja and D. Loss, Fractional charge and spin states in topological insulator constrictions, *Phys. Rev. B* **92**, 121410 (2015).
- [71] H. Ebisu, B. Lu, J. Klinovaja, and Y. Tanaka, Theory of time-reversal topological superconductivity in double Rashba wires: symmetries of Cooper pairs and Andreev bound states, *Prog. Theo. Exp. Phys.* **2016**, 083101 (2016).
- [72] C. Schrade, M. Thakurathi, C. Reeg, S. Hoffman, J. Klinovaja, and D. Loss, Low-field topological threshold in Majorana double nanowires, *Phys. Rev. B* **96**, 035306 (2017).
- [73] M. Thakurathi, P. Simon, I. Mandal, J. Klinovaja, and D. Loss, Majorana Kramers pairs in Rashba double nanowires with interactions and disorder, *Phys. Rev. B* **97**, 045415 (2018).
- [74] W. A. Benalcazar, B. A. Bernevig, and T. L. Hughes, Quantized electric multipole insulators, *Science* **357**, 61 (2017).
- [75] W. A. Benalcazar, B. A. Bernevig, and T. L. Hughes, Electric multipole moments, topological multipole moment pumping, and chiral hinge states in crystalline insulators, *Phys. Rev. B* **96**, 245115 (2017).
- [76] F. Schindler, A. M. Cook, M. G. Vergniory, Z. Wang, S. S. P. Parkin, B. A. Bernevig, and T. Neupert, Higher-order topological insulators, *Sci. Adv.* **4**, eaat0346 (2018).
- [77] J. Langbehn, Y. Peng, L. Trifunovic, F. von Oppen, and P. W. Brouwer, Reflection-Symmetric Second-Order Topological Insulators and Superconductors, *Phys. Rev. Lett.* **119**, 246401 (2017).
- [78] Z. Song, Z. Fang, and C. Fang, $(d-2)$ -Dimensional Edge States of Rotation Symmetry Protected Topological States, *Phys. Rev. Lett.* **119**, 246402 (2017).
- [79] M. Ezawa, Higher-Order Topological Insulators and Semimetals on the Breathing Kagome and Pyrochlore Lattices, *Phys. Rev. Lett.* **120**, 026801 (2018).
- [80] F. Schindler, Z. Wang, M. G. Vergniory, A. M. Cook, A. Murani, S. Sengupta, A. Y. Kasumov, R. Deblock, S. Jeon, I. Drozdov, H. Bouchiat, S. Guéron, A. Yazdani, B. A. Bernevig, and T. Neupert, Higher-order topology in bismuth,

- Nat. Phys. (2018), 10.1038/s41567-018-0224-7.
- [81] E. Khalaf, Higher-order topological insulators and superconductors protected by inversion symmetry, *Phys. Rev. B* **97**, 205136 (2018).
- [82] C. Beenakker, Mystery solved of the sawtooth Josephson effect in bismuth, <https://www.condmat.jclub.org/?p=3319> (2018).
- [83] L. Fu, C. L. Kane, and E. J. Mele, Topological Insulators in Three Dimensions, *Phys. Rev. Lett.* **98**, 106803 (2007).
- [84] J. E. Moore and L. Balents, Topological invariants of time-reversal-invariant band structures, *Phys. Rev. B* **75**, 121306 (2007).
- [85] D. Hsieh, D. Qian, L. Wray, Y. Xia, Y. S. Hor, R. J. Cava, and M. Z. Hasan, A topological Dirac insulator in a quantum spin Hall phase, *Nature* **452**, 970 (2008).
- [86] R. Roy, Topological phases and the quantum spin Hall effect in three dimensions, *Phys. Rev. B* **79**, 195322 (2009).
- [87] C. L. Kane and E. J. Mele, Z_2 topological order and the quantum spin Hall effect, *Phys. Rev. Lett.* **95**, 146802 (2005).
- [88] C. L. Kane and E. J. Mele, Quantum Spin Hall Effect in Graphene, *Phys. Rev. Lett.* **95**, 226801 (2005).
- [89] B. A. Bernevig and S.-C. Zhang, Quantum Spin Hall Effect, *Phys. Rev. Lett.* **96**, 106802 (2006).
- [90] B. A. Bernevig, T. L. Hughes, and S.-C. Zhang, Quantum Spin Hall Effect and Topological Phase Transition in HgTe Quantum Wells, *Science* **314**, 1757 (2006).
- [91] S. Murakami, Quantum Spin Hall Effect and Enhanced Magnetic Response by Spin-Orbit Coupling, *Phys. Rev. Lett.* **97**, 236805 (2006).
- [92] C. Liu, T. L. Hughes, X.-L. Qi, K. Wang, and S.-C. Zhang, Quantum Spin Hall Effect in Inverted Type-II Semiconductors, *Phys. Rev. Lett.* **100**, 236601 (2008).
- [93] M. Wada, S. Murakami, F. Freimuth, and G. Bihlmayer, Localized edge states in two-dimensional topological insulators: Ultrathin Bi films, *Phys. Rev. B* **83**, 121310 (2011).
- [94] I. K. Drozdov, A. Alexandradinata, S. Jeon, S. Nadj-Perge, H. Ji, R. J. Cava, B. A. Bernevig, and A. Yazdani, One-dimensional topological edge states of bismuth bilayers, *Nat. Phys.* **10**, 664 (2014).
- [95] A. Murani, A. Kasumov, S. Sengupta, Y. A. Kasumov, V. T. Volkov, I. I. Khodos, F. Brisset, R. Delagrangé, A. Chepelianskii, R. Deblock, H. Bouchiat, and S. Guéron, Ballistic edge states in Bismuth nanowires revealed by SQUID interferometry, *Nat. Commun.* **8**, 15941 (2017).
- [96] See Supplemental Material at [URL will be inserted by publisher] for the technical details, which include Refs. [126, 127].
- [97] J. Klinovaja and D. Loss, Composite Majorana fermion wave functions in nanowires, *Phys. Rev. B* **86**, 085408 (2012).
- [98] C. Reeg, J. Klinovaja, and D. Loss, Destructive interference of direct and crossed Andreev pairing in a system of two nanowires coupled via an s -wave superconductor, *Phys. Rev. B* **96**, 081301 (2017).
- [99] C.-H. Hsu, P. Stano, J. Klinovaja, and D. Loss, Nuclear-spin-induced localization of edge states in two-dimensional topological insulators, *Phys. Rev. B* **96**, 081405 (2017).
- [100] C.-H. Hsu, P. Stano, J. Klinovaja, and D. Loss, Effects of nuclear spins on the transport properties of the edge of two-dimensional topological insulators, *Phys. Rev. B* **97**, 125432 (2018).
- [101] T. Giamarchi, *Quantum Physics in One Dimension* (Oxford University Press, New York, 2003).
- [102] S. Gangadharaiah, B. Braunecker, P. Simon, and D. Loss, Majorana Edge States in Interacting One-Dimensional Systems, *Phys. Rev. Lett.* **107**, 036801 (2011).
- [103] J. Maciejko, C. Liu, Y. Oreg, X.-L. Qi, C. Wu, and S.-C. Zhang, Kondo effect in the helical edge liquid of the quantum spin Hall state, *Phys. Rev. Lett.* **102**, 256803 (2009).
- [104] P. Virtanen and P. Recher, Signatures of Rashba spin-orbit interaction in the superconducting proximity effect in helical Luttinger liquids, *Phys. Rev. B* **85**, 035310 (2012).
- [105] Y. M. Koroteev, G. Bihlmayer, E. V. Chulkov, and S. Blügel, First-principles investigation of structural and electronic properties of ultrathin Bi films, *Phys. Rev. B* **77**, 045428 (2008).
- [106] P. Recher, E. V. Sukhorukov, and D. Loss, Andreev tunneling, Coulomb blockade, and resonant transport of nonlocal spin-entangled electrons, *Phys. Rev. B* **63**, 165314 (2001).
- [107] P. Recher and D. Loss, Superconductor coupled to two Luttinger liquids as an entangler for electron spins, *Phys. Rev. B* **65**, 165327 (2002).
- [108] C. Bena, S. Vishveshwara, L. Balents, and M. P. A. Fisher, Quantum Entanglement in Carbon Nanotubes, *Phys. Rev. Lett.* **89**, 037901 (2002).
- [109] L. Hofstetter, S. Csonka, J. Nygård, and C. Schönenberger, Cooper pair splitter realized in a two-quantum-dot Y-junction, *Nature* **461**, 960 (2009).
- [110] K. Sato, D. Loss, and Y. Tserkovnyak, Cooper-Pair Injection into Quantum Spin Hall Insulators, *Phys. Rev. Lett.* **105**, 226401 (2010).
- [111] L. Hofstetter, S. Csonka, A. Baumgartner, G. Fülöp, S. d'Hollosy, J. Nygård, and C. Schönenberger, Finite-Bias Cooper Pair Splitting, *Phys. Rev. Lett.* **107**, 136801 (2011).
- [112] K. Sato, D. Loss, and Y. Tserkovnyak, Crossed Andreev reflection in quantum wires with strong spin-orbit interaction, *Phys. Rev. B* **85**, 235433 (2012).
- [113] J. Schindele, A. Baumgartner, and C. Schönenberger, Near-Unity Cooper Pair Splitting Efficiency, *Phys. Rev. Lett.* **109**, 157002 (2012).
- [114] A. Das, Y. Ronen, M. Heiblum, D. Mahalu, A. V. Kretinin, and H. Shtrikman, High-efficiency Cooper pair splitting demonstrated by two-particle conductance resonance and positive noise cross-correlation, *Nat. Commun.* **3**, 1165 (2012).
- [115] G. Fülöp, S. d'Hollosy, A. Baumgartner, P. Makk, V. A. Guzenko, M. H. Madsen, J. Nygård, C. Schönenberger, and S. Csonka, Local electrical tuning of the nonlocal signals in a Cooper pair splitter, *Phys. Rev. B* **90**, 235412 (2014).
- [116] G. Fülöp, F. Domínguez, S. d'Hollosy, A. Baumgartner, P. Makk, M. H. Madsen, V. A. Guzenko, J. Nygård, C. Schönenberger, A. Levy Yeyati, and S. Csonka, Magnetic Field Tuning and Quantum Interference in a Cooper Pair Splitter, *Phys. Rev. Lett.* **115**, 227003 (2015).
- [117] R. S. Deacon, A. Oiwa, J. Sailer, S. Baba, Y. Kanai, K. Shibata, K. Hirakawa, and S. Tarucha, Cooper pair splitting in parallel quantum dot Josephson junctions, *Nat. Commun.* **6**, 7446 (2015).
- [118] S. Baba, C. Jünger, S. Matsuo, A. Baumgartner, Y. Sato, H. Kamata, K. Li, S. Jeppesen, L. Samuelson, H. Q. Xu, C. Schönenberger, and S. Tarucha, Cooper-pair splitting in two parallel InAs nanowires, *New J. Phys.* **20**, 063021 (2018).
- [119] C. Schrade and L. Fu, Parity-Controlled 2π Josephson Effect Mediated by Majorana Kramers Pairs, *Phys. Rev. Lett.* **120**, 267002 (2018).
- [120] X.-J. Liu, C. L. M. Wong, and K. T. Law, Non-Abelian Majorana Doublets in Time-Reversal-Invariant Topological Superconductors, *Phys. Rev. X* **4**, 021018 (2014).
- [121] P. Gao, Y.-P. He, and X.-J. Liu, Symmetry-protected non-Abelian braiding of Majorana Kramers pairs, *Phys. Rev. B* **94**, 224509 (2016).
- [122] C. Schrade and L. Fu, Quantum Computing with

- Majorana Kramers Pairs, ArXiv e-prints (2018), arXiv:1807.06620 [cond-mat.mes-hall].
- [123] L. A. Landau, S. Plugge, E. Sela, A. Altland, S. M. Albrecht, and R. Egger, Towards Realistic Implementations of a Majorana Surface Code, *Phys. Rev. Lett.* **116**, 050501 (2016).
- [124] S. Hoffman, C. Schrade, J. Klinovaja, and D. Loss, Universal quantum computation with hybrid spin-Majorana qubits, *Phys. Rev. B* **94**, 045316 (2016).
- [125] T. Karzig, C. Knapp, R. M. Lutchyn, P. Bonderson, M. B. Hastings, C. Nayak, J. Alicea, K. Flensberg, S. Plugge, Y. Oreg, C. M. Marcus, and M. H. Freedman, Scalable designs for quasiparticle-poisoning-protected topological quantum computation with majorana zero modes, *Phys. Rev. B* **95**, 235305 (2017).
- [126] T. L. Schmidt, S. Rachel, F. von Oppen, and L. I. Glazman, Inelastic Electron Backscattering in a Generic Helical Edge Channel, *Phys. Rev. Lett.* **108**, 156402 (2012).
- [127] M. G. Vergniory, L. Elcoro, C. Felser, B. A. Bernevig, and Z. Wang, The (High Quality) Topological Materials In The World, ArXiv e-prints (2018), arXiv:1807.10271 [cond-mat.mtrl-sci]

Supplemental Material to “Majorana Kramers pairs in higher-order topological insulators”

Chen-Hsuan Hsu¹, Peter Stano^{1,2,3}, Jelena Klinovaja^{1,4}, and Daniel Loss^{1,4}

¹RIKEN Center for Emergent Matter Science (CEMS), Wako, Saitama 351-0198, Japan

²Department of Applied Physics, School of Engineering, University of Tokyo, 7-3-1 Hongo, Bunkyo-ku, Tokyo 113-8656, Japan

³Institute of Physics, Slovak Academy of Sciences, 845 11 Bratislava, Slovakia

⁴Department of Physics, University of Basel, Klingelbergstrasse 82, CH-4056 Basel, Switzerland

CONTENTS

I. Pairing processes and decoupling of the third hinge	1
II. Wave functions of the Majorana Kramers pair	2
III. Effects of the intra-/inter-hinge coupling and the spin-orbit interactions	3
IV. RG analysis from the effective Hamiltonian method	3
V. Source-term approach using a microscopic model	4
VI. Feasibility of the proposed scheme	6

I. Pairing processes and decoupling of the third hinge

In this Section we discuss the pairing processes within/between the three helical hinges, and show that the third, middle parallel, hinge is trivially gapped and decoupled from the other hinges (1 and 2). We describe the three hinge states by the fields,

$$\psi_n(r) = \psi_{n,\downarrow}(r) + \psi_{n,\uparrow}(r) \quad \text{for } n \in \{1, 2, 3\}, \quad (\text{S1a})$$

$$\psi_{n,\uparrow}(r) = L_{n,\uparrow}(r)e^{-ik_F r} \quad \text{for } n \in \{1, 2\}, \quad (\text{S1b})$$

$$\psi_{n,\downarrow}(r) = R_{n,\downarrow}(r)e^{ik_F r} \quad \text{for } n \in \{1, 2\}, \quad (\text{S1c})$$

$$\psi_{3,\uparrow}(r) = R_{3,\uparrow}(r)e^{ik_F r}, \quad (\text{S1d})$$

$$\psi_{3,\downarrow}(r) = L_{3,\downarrow}(r)e^{-ik_F r}, \quad (\text{S1e})$$

with the coordinate r along the hinge, the Fermi wave number k_F , and the slowly varying right- and left-moving fields $R_{n,\sigma}$ and $L_{n,\sigma}$ (the spin index $\sigma \in \{\uparrow, \downarrow\}$), respectively. A Bardeen–Cooper–Schrieffer (BCS) type pairing term between the hinges n and n' is in the form of

$$\propto [\psi_{n,\downarrow}^\dagger(-k)\psi_{n',\uparrow}^\dagger(k) + \text{H.c.}], \quad (\text{S2})$$

with the momentum k , which puts constraints on the momenta and spins of the allowed pairs. Namely, for the electrons to be paired, they must possess zero total momentum and opposite spins. The pairing processes within/between the three helical hinges are sketched in Fig. S1. The local pairing terms ($n = n'$) for hinges 1 and 2 are given by Eq. (3) in the main text, and, for hinge 3, it is given by

$$H_3 = \int dr \left[\frac{\Delta_3}{2} (R_{3,\uparrow}^\dagger L_{3,\downarrow}^\dagger - L_{3,\downarrow}^\dagger R_{3,\uparrow}^\dagger) + \text{H.c.} \right], \quad (\text{S3})$$

with the local pairing gap Δ_3 . These terms are indicated by the black dotted arrows in Fig. S1.

On the other hand, the nonlocal (crossed Andreev) pairing term ($n \neq n'$) requires more caution. Due to the identical

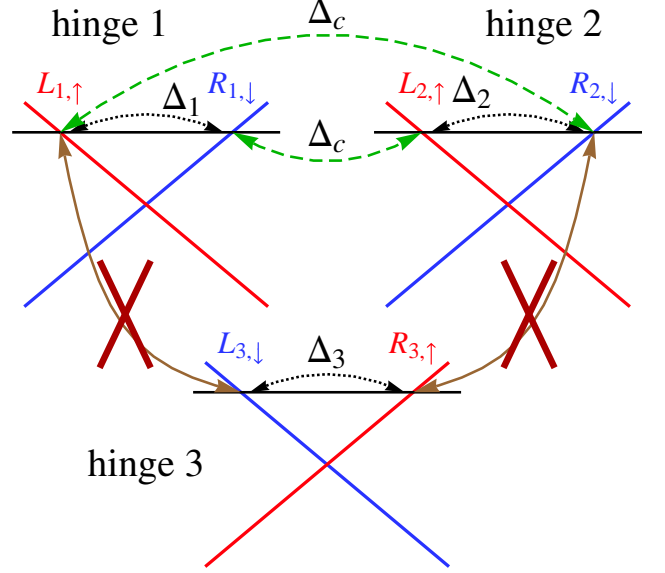


FIG. S1. Schematics of the pairing processes in momentum space. The hinges 1 and 2 carry the same helicity (a given spin state in both of the hinges move in the same direction) while the hinge 3 has the opposite helicity. The local pairing (black dotted arrows, Δ_n) occurs within the hinges. The crossed Andreev pairing (green dashed arrows, Δ_c) is allowed only between the hinges 1 and 2, and forbidden between the other pairs due to the momentum mismatch.

chemical potential of the hinges, the pairing between the parallel hinges (1 and 2) is allowed, which is described by the green dashed arrows in Fig. S1 [see Eq. (4) in the main text], whereas the corresponding terms between the hinges 3 and $n \in \{1, 2\}$ are given by

$$\int dr \left\{ (R_{n,\downarrow}^\dagger R_{3,\uparrow}^\dagger e^{-2ik_F r} + L_{3,\downarrow}^\dagger L_{n,\uparrow}^\dagger e^{2ik_F r}) + \text{H.c.} \right\}. \quad (\text{S4})$$

The integral in Eq. (S4) contains a fast oscillating integrand, and vanishes for $k_F L \gg 1$. As a result, the crossed Andreev pairing between the third hinge and the others is suppressed due to the momentum mismatch, so we can describe the two subsystems separately. To be specific, we describe the whole system of the three hinges by the total Hamiltonian, $H_{\text{tot}} =$

$H + H_3$, which is block-diagonalized into two parts,

$$H = \frac{1}{2} \int dr \Psi^\dagger(r) \mathcal{H}(r) \Psi(r), \quad (\text{S5a})$$

$$H_3 = \frac{1}{2} \int dr \Psi_3^\dagger(r) \mathcal{H}_3(r) \Psi_3(r), \quad (\text{S5b})$$

with the basis

$$\Psi = (R_{1,\downarrow}, L_{1,\uparrow}, R_{2,\downarrow}, L_{2,\uparrow}, R_{1,\downarrow}^\dagger, L_{1,\uparrow}^\dagger, R_{2,\downarrow}^\dagger, L_{2,\uparrow}^\dagger)^\text{T}, \quad (\text{S6a})$$

$$\Psi_3 = (R_{3,\uparrow}, L_{3,\downarrow}, R_{3,\uparrow}^\dagger, L_{3,\downarrow}^\dagger)^\text{T}. \quad (\text{S6b})$$

The Hamiltonian density \mathcal{H} in the subspace of hinges 1 and 2 is given in Eq. (5) in the main text. In the subspace of hinge 3, we have

$$\mathcal{H}_3(r) = -i\hbar v_F \eta^0 \sigma^z \partial_r - \Delta_3 \eta^y \sigma^y, \quad (\text{S7})$$

so the third hinge is trivially gapped by the local pairing, and decoupled from the others. This allows us to focus on the two hinges that are parahalical to each other. We therefore present an effective model \mathcal{H} for the two parahalical hinges of interest (1 and 2) in the main text.

In the above, we take the same Fermi wave number for the parahalical hinges 1 and 2 based on the following considerations. First, the chemical potential is uniform along the hinges, since they are all connected. Second, the bismuth crystal structure respects the three-fold rotational symmetry around the (111) axis [S1]. The two parahalical hinges, which are related to each other by such a rotation, are therefore characterized by the same energy band, as implied by the C_3 rotational symmetry of the underlying crystal structure; see Ref. [S1] for the degenerate hinge-state energy bands calculated from their tight-binding model.

Local disorder may, however, alter the energy bands of the hinge states, and therefore modify the Fermi wave numbers. As a result, a difference between the Fermi wave numbers of the two hinges will reduce the crossed Andreev pairing. Such an effect can be straightforwardly incorporated in our model, by starting with a larger ratio of Δ_1/Δ_c in the renormalization-group (RG) analysis. Assuming the perturbations are small (weak disorder) so that the suppression is not complete, the Majorana Kramers pairs will still be stabilized (even though stronger electron-electron interactions are then required), and our conclusions remain qualitatively unchanged.

II. Wave functions of the Majorana Kramers pair

In this Section we give the bulk spectrum of the single-particle Hamiltonian $\mathcal{H}(r)$ in Eq. (5), and the corresponding wave functions of the Majorana Kramers pair localized at the boundary $r = 0$. Upon replacement $-i\partial_r \rightarrow k$ in $\mathcal{H}(r)$ and

diagonalization, we find the two-fold degenerate bulk spectrum

$$E_{\text{bulk}}^{(\pm, \pm)}(k) = \pm \left[\hbar^2 v_F^2 k^2 + \left(\Delta_+ \pm \sqrt{\Delta_-^2 + \Delta_c^2} \right)^2 \right]^{1/2}, \quad (\text{S8})$$

which has a gap at $k = 0$. To be specific, we define the bulk gap as

$$\begin{aligned} \Delta_b &\equiv E_{\text{bulk}}^{(+, -)}(k=0) - E_{\text{bulk}}^{(-, -)}(k=0) \\ &= 2 \left(\Delta_+ - \sqrt{\Delta_-^2 + \Delta_c^2} \right). \end{aligned} \quad (\text{S9})$$

Assuming $\Delta_1, \Delta_2 > 0$, the sign of Δ_b is given by the sign of

$$\Delta_1 \Delta_2 - \Delta_c^2, \quad (\text{S10})$$

indicating that the bulk gap Δ_b changes its sign when the local and crossed Andreev pairings reverse their relative strengths.

We remark that, for Δ_1 and Δ_2 with general signs, Δ_b can reverse its sign without involving the crossed Andreev pairing. It can be demonstrated by setting $\Delta_c = 0$ in Eq. (S9). In this case, Δ_b becomes negative when the signs of Δ_1 and Δ_2 are opposite (π -junction). In our setup, the phase of Δ_1 and Δ_2 is the same, as they both stem from a single parent superconductor. An interesting scenario of a π -junction[S2–S8] would require a different setup. In the main text, we therefore focus on the case where Δ_1 and Δ_2 are both positive.

We now turn to the wave functions of the Majorana Kramers pair. When $\Delta_c^2 > \Delta_1 \Delta_2$, we find that a Kramers pair of Majorana bound states emerges at the boundary $r = 0$, with the wave functions $\Phi_{\text{MF},1}$ and $\Phi_{\text{MF},2}$. In the basis of $\Psi = (R_1, L_1, R_2, L_2, R_1^\dagger, L_1^\dagger, R_2^\dagger, L_2^\dagger)^\text{T}$, we have $\Phi_{\text{MF},1}(r) = \Phi_>(r)\Theta(r) + \Phi_<(r)\Theta(-r)$, with the step function $\Theta(r)$ and

$$\Phi_>(r) = e^{-\kappa r} \times (i\eta, -\eta, -i, 1, -i\eta, -\eta, i, 1)^\text{T}, \quad (\text{S11a})$$

$$\begin{aligned} \Phi_<(r) = &(i\eta e^{\kappa_1 r}, -\eta e^{\kappa_1 r}, -i e^{\kappa_2 r}, e^{\kappa_2 r}, \\ &-i\eta e^{\kappa_1 r}, -\eta e^{\kappa_1 r}, i e^{\kappa_2 r}, e^{\kappa_2 r})^\text{T}, \end{aligned} \quad (\text{S11b})$$

where the normalization constants of $\Phi_>(r)$ and $\Phi_<(r)$ were omitted, and

$$\eta = \frac{\sqrt{\Delta_-^2 + \Delta_c^2} - \Delta_-}{\Delta_c}, \quad (\text{S12a})$$

$$\kappa = \frac{\sqrt{\Delta_-^2 + \Delta_c^2} - \Delta_+}{\hbar v_F}, \quad (\text{S12b})$$

$$\kappa_n = \frac{\Delta_n}{\hbar v_F} \text{ for } n \in \{1, 2\}. \quad (\text{S12c})$$

The localization length of the Majorana bound states is thus given by

$$\xi_{\text{loc}} = \frac{1}{\min(\kappa, \kappa_1, \kappa_2)}, \quad (\text{S13})$$

which is estimated in Sec. IV. The second Majorana wave function is related to its Kramers partner by $\Phi_{\text{MF},2} = \mathcal{T}\Phi_{\text{MF},1}$ with the time-reversal operator $\mathcal{T} = i\sigma^y\mathcal{K}$ and the complex conjugate operator \mathcal{K} . We note that the two Majorana wave functions also satisfy the relation $\Phi_{\text{MF},1} = -\mathcal{T}\Phi_{\text{MF},2}$, such that $\mathcal{T}^2 = -1$, as required for spin-1/2 particles. One can check that $\Phi_{\text{MF},1}$ and $\Phi_{\text{MF},2}$ are orthogonal, as guaranteed by the Kramers degeneracy theorem. Therefore, even though they are not spatially separated, they do not hybridize into an ordinary fermion as long as time-reversal symmetry is preserved.

III. Effects of the intra-/inter-hinge coupling and the spin-orbit interactions

In this Section we discuss the effects of the intra-hinge and inter-hinge couplings, as well as the spin-orbit interactions. In addition to the pairing processes discussed in the main text, the single-particle intra-hinge (inter-hinge) coupling can also arise from the second-order spin-conserving (co-)tunneling processes within (between) hinges 1 and 2. We note that the effects of similar processes have been discussed in nonhelical systems [S9, S10] and in the helical edge channels of two-dimensional topological insulators [S11, S12].

To proceed, we incorporate the following terms

$$H_{\delta\mu} = -\delta\mu \sum_{n=1,2} \sum_{\sigma=\uparrow,\downarrow} \int dr \psi_{n,\sigma}^\dagger(r) \psi_{n,\sigma}(r), \quad (\text{S14})$$

$$H_\Gamma = -\Gamma \sum_{\sigma=\uparrow,\downarrow} \int dr [\psi_{1,\sigma}^\dagger(r) \psi_{2,\sigma}(r) + \text{H.c.}], \quad (\text{S15})$$

into the single-particle Hamiltonian given in the main text. To be explicit, we replace the Hamiltonian density [Eq. (5) in the main text] with

$$\mathcal{H} \rightarrow \mathcal{H} - \delta\mu \eta^z \tau^0 \sigma^0 - \Gamma \eta^z \tau^x \sigma^0 \quad (\text{S16})$$

with the Pauli matrices defined as in the main text. The effective couplings $\delta\mu$ and Γ are of the second order in the tunnel coupling between the hinges and the superconductor. The derivations of the explicit forms of $\delta\mu$ and Γ can be nontrivial [S9, S10]. Instead of aiming at the derivation, we treat them as effective parameters, and show that they do not affect the topological criterion.

The bulk spectrum of the full Hamiltonian [with the Hamiltonian density in Eq. (S16)] is given by $\pm E_b^{(\eta,\pm)}(k)$, with

$$E_b^{(\eta,\pm)}(k) = \left[\xi_\eta^2(k) + \Delta_1^2 + \Delta_c^2 + \Gamma^2 \pm 2|\xi_\eta(k)\Gamma + \eta\Delta_1\Delta_c| \right]^{1/2}, \quad (\text{S17})$$

where we define $\xi_\eta(k) \equiv \hbar v_F k + \eta\delta\mu$ with $\eta \in \{+, -\}$ and set $\Delta_1 = \Delta_2$ for simplicity. We note that the bulk spectrum remains two-fold degenerate at the time-reversal-invariant momentum $k = 0$. From the above equation, we see

that, for general Γ and $\delta\mu$, the band-touching points shift from $k = 0$ to the points associated with $\xi_\eta^2(k) = \Gamma^2$. Important for us, however, the system gap remains to be $|\Delta_c - \Delta_1|$ (assuming $\Delta_1, \Delta_c > 0$), indicating the same gap closing point and therefore the same phase transition point in the parameter space

$$\Delta_c = \Delta_1, \quad (\text{S18})$$

as in the limit of $\Gamma = \delta\mu = 0$. As a consequence, the nonzero Γ and $\delta\mu$ do not lead to the system gap closing or reopening, so that the Majorana Kramers pairs in the $\Delta_c > \Delta_1$ regime are robust against the intra-hinge and inter-hinge couplings as long as the pairing gaps Δ_n are not drastically different.

Furthermore, it was shown in Ref. [S11] that when the electron-electron interactions are taken into account, the crossed Andreev pairing is the most relevant term in the RG sense (justified by the scaling dimension). As a result, the additional tunneling processes are less important than the crossed Andreev pairing, and can be safely neglected in interacting systems. To conclude, while the intra-hinge and inter-hinge couplings alter the bulk spectrum, they do not destabilize the Majorana Kramers pairs.

Finally, it may be interesting to examine the effects of the spin-orbit interactions arising from, say, substrates or gate-induced electric field. In principle, these Rashba-type spin-orbit interactions may affect the spins of the hinge states, similarly to edge states of two-dimensional topological insulators [S13]. While the detailed analysis on their effects is beyond the scope of this work, we make two remarks here. First, as mentioned in the main text, due to its self-tuned nature, our setup does not require local gates, thereby minimizing the Rashba-type spin-orbit interactions. Second, since the spin-orbit interactions respect time-reversal symmetry, there are still Kramers partners of the hinge states. Consequently, the spin states of the left- and right-movers in a given hinge remain strictly orthogonal, so the pairing processes are not affected by the spin-orbit interactions. Concluding, the presence of either the intra-/inter-hinge coupling or the spin-orbit interactions does not alter our conclusions.

IV. RG analysis from the effective Hamiltonian method

In this Section we outline our RG analysis using the effective Hamiltonian method. First, we introduce the boson fields θ_n and ϕ_n used to bosonize the Hamiltonian in an interacting system. They are related to the fermion fields R_n and L_n through (with the hinge index $n \in \{1, 2\}$) [S14, S15]

$$R_n(r) = \frac{U_R}{\sqrt{2\pi a}} e^{i[-\phi_n(r) + \theta_n(r)]}, \quad (\text{S19a})$$

$$L_n(r) = \frac{U_L}{\sqrt{2\pi a}} e^{i[\phi_n(r) + \theta_n(r)]}, \quad (\text{S19b})$$

where U_R and U_L are the Klein factors, and a is the short-distance cutoff, taken to be the transverse decay length of the

hinge states. The formulas (S19) are used to derive Eqs. (7), (8), and (9) in the main text.

Next, we present the RG flow equations derived from the effective Hamiltonian method [see Eqs. (7), (8), and (9) in the main text]. Since Eq. (9) contains the fields ϕ_n while Eq. (8) contains their conjugate fields θ_n , the two types of pairing processes compete with each other [S16]. We then expect that their relative strength varies with the interaction strength, as we demonstrate below.

To this end, we construct the RG flow equations by computing the correlation function, and changing the cut-off $a \rightarrow a(l) = a(0)e^l$ with the dimensionless scale $l = \ln[a(l)/a(0)]$ [S16]. We obtain

$$\frac{d\tilde{\Delta}_1(l)}{dl} = \left[2 - \frac{1}{K_1(l)} \right] \tilde{\Delta}_1(l), \quad (\text{S20a})$$

$$\frac{d\tilde{\Delta}_2(l)}{dl} = \left[2 - \frac{1}{K_2(l)} \right] \tilde{\Delta}_2(l), \quad (\text{S20b})$$

$$\frac{d\tilde{\Delta}_c(l)}{dl} = \left[2 - \frac{1}{4} \left(K_1(l) + K_2(l) + \frac{1}{K_1(l)} + \frac{1}{K_2(l)} \right) \right] \times \tilde{\Delta}_c(l), \quad (\text{S20c})$$

$$\frac{dK_1(l)}{dl} = \tilde{\Delta}_1^2(l) + \frac{1}{2} [1 - K_1^2(l)] \tilde{\Delta}_c^2(l), \quad (\text{S20d})$$

$$\frac{dK_2(l)}{dl} = \tilde{\Delta}_2^2(l) + \frac{1}{2} [1 - K_2^2(l)] \tilde{\Delta}_c^2(l), \quad (\text{S20e})$$

where the dimensionless coupling constants are given by

$$\tilde{\Delta}_1(l) = \frac{\Delta_1(l)a(l)}{\hbar u_1}, \quad (\text{S21a})$$

$$\tilde{\Delta}_2(l) = \frac{\Delta_2(l)a(l)}{\hbar u_2}, \quad (\text{S21b})$$

$$\tilde{\Delta}_c(l) = \frac{\Delta_c(l)a(l)}{\hbar \sqrt{u_1 u_2}}. \quad (\text{S21c})$$

Several remarks on Eqs. (S20) are in order. First, both types of dimensionful pairing gaps Δ_n and Δ_c are suppressed by a repulsive interaction $K_n(0) < 1$. Second, due to the different scaling dimensions of the cosine terms in Eqs. (8)–(9), the local pairing gap is suppressed more significantly than the crossed Andreev pairing. Therefore, the repulsive interaction favors the nonlocal pairing process, similarly as in nonhelical nanowires [S17]. Third, from Eqs. (S20), we see that, for $K_1(0) = K_2(0) < 2 - \sqrt{3} \approx 0.27$, both $\tilde{\Delta}_{1,2}$ and $\tilde{\Delta}_c$ are irrelevant in the RG sense. Namely, both of the gaps flow to zero, so the hinge states remain non-superconducting in the presence of a very strong electron-electron interaction.

The RG flow equations Eqs. (S20) are numerically solved using the initial conditions,

$$\tilde{\Delta}_1(0) \equiv \tilde{\Delta}_1(l=0) = \tilde{\Delta}_2(l=0), \quad (\text{S22a})$$

$$\tilde{\Delta}_c(0) \equiv \tilde{\Delta}_c(l=0), \quad (\text{S22b})$$

$$K_1(0) \equiv K_1(l=0) = K_2(l=0). \quad (\text{S22c})$$

The RG flow is stopped whenever any of the dimensionless coupling constants becomes unity, including also the interaction parameters K_n and the dimensionless system size $a(l)/L$ with the hinge length L . The main results of the numerical

calculation are presented in Figs. 3 and 4, and discussed in the main text. Moreover, the renormalized values of the pairing gaps allow us to obtain the localization length. Using Eq. (S13) and the initial parameters $K_1(0) = K_2(0) = 0.6$ – 0.7 , $\tilde{\Delta}_1(0) = \tilde{\Delta}_2(0) = 0.03$, $\tilde{\Delta}_c(0) = 0.01$, and $a(0) = 5$ nm, we get $\xi_{\text{loc}} = 19$ – 21 nm, which is much shorter than the hinge length $L \sim O(\mu\text{m})$, and justifies that the Majorana bound states located at $r = 0$ and $r = L$ do not overlap.

In comparison with nonhelical (spin-degenerate) nanowires [S17], our setup requires weaker interactions for Majorana Kramers pairs. This quantitative difference between the nonhelical and helical channels can be understood as discussed in Refs. [S14, S15]. Namely, in a nonhelical system, the effects of the electron-electron interactions are “averaged” over the charge and (noninteracting) spin sectors, and thus weakened compared to a helical one. Consequently, it requires stronger interactions in the charge sector of a nonhelical channel to drive the system into the regime hosting Majorana Kramers pairs. It suggests that the helical hinge states of higher-order topological insulators offer a promising platform for topological superconductivity without magnetic fields.

V. Source-term approach using a microscopic model

In this Section we present the RG flow equations and phase diagram obtained from the source-term approach [S17, S18], supplementary to the effective Hamiltonian method presented in the main text. We assume a weak tunnel coupling between the hinge states and a proximity BCS superconductor, described by the tunnel Hamiltonian

$$H_T = \sum_{n=1,2} \int dr d\mathbf{R} \left\{ t'_n(r, \mathbf{R}) \left[R_n^\dagger(r) \psi_{s,\downarrow}(\mathbf{R}) + L_n^\dagger(r) \psi_{s,\uparrow}(\mathbf{R}) \right] + \text{H.c.} \right\}. \quad (\text{S23})$$

Here, \mathbf{R} is the three-dimensional coordinate in the bulk of the superconductor, and $\psi_{s,\sigma}$ is the annihilation operator with spin σ in the superconductor. We take the tunnel amplitude t'_n to be in the form of the three-dimensional delta function,

$$t'_n(r, \mathbf{R}) \equiv t_n \delta(R_z - r) \delta(R_x - d_n) \delta(R_y), \quad (\text{S24a})$$

with $d_1 = d/2$ and $d_2 = -d/2$, where d is the distance between the two hinges. The BCS Hamiltonian describing the superconductor is given by

$$H_{\text{BCS}} = \sum_{\mathbf{k}, \sigma=\uparrow, \downarrow} \frac{\hbar^2(k^2 - k_{F_s}^2)}{2m_e} \psi_{s,\sigma}^\dagger(\mathbf{k}) \psi_{s,\sigma}(\mathbf{k}) + \Delta_s \sum_{\mathbf{k}} \psi_{s,\uparrow}(\mathbf{k}) \psi_{s,\downarrow}(-\mathbf{k}) + \text{H.c.}, \quad (\text{S25})$$

with the electron mass m_e , the BCS pairing gap Δ_s , and the Fermi wave number k_{F_s} of the superconductor in its normal phase.

To proceed, we first integrate out the field $\psi_{s,\sigma}$ in $H_{\text{BCS}} + H_{\text{T}}$ to obtain the effective action [S9], and then construct the RG flow equations following Refs. [S16–S18]. The result is summarized as follows,

$$\frac{d\tilde{t}_1(l)}{dl} = \left[2 - \frac{1}{4} \left(K_1(l) + \frac{1}{K_1(l)} \right) \right] \tilde{t}_1(l), \quad (\text{S26a})$$

$$\frac{d\tilde{t}_2(l)}{dl} = \left[2 - \frac{1}{4} \left(K_2(l) + \frac{1}{K_2(l)} \right) \right] \tilde{t}_2(l), \quad (\text{S26b})$$

$$\frac{d\tilde{\Delta}_1(l)}{dl} = \left[2 - \frac{1}{K_1(l)} \right] \tilde{\Delta}_1(l) + S_1(l)\tilde{t}_1^2(l), \quad (\text{S26c})$$

$$\frac{d\tilde{\Delta}_2(l)}{dl} = \left[2 - \frac{1}{K_2(l)} \right] \tilde{\Delta}_2(l) + S_2(l)\tilde{t}_2^2(l), \quad (\text{S26d})$$

$$\frac{d\tilde{\Delta}_c(l)}{dl} = \left[2 - \frac{1}{4} \left(K_1(l) + K_2(l) + \frac{1}{K_1(l)} + \frac{1}{K_2(l)} \right) \right] \tilde{\Delta}_c(l) + S_c(l)\tilde{t}_1(l)\tilde{t}_2(l), \quad (\text{S26e})$$

$$\frac{dK_1(l)}{dl} = \tilde{\Delta}_1^2(l) + \frac{1}{2} [1 - K_1^2(l)] \tilde{\Delta}_c^2(l), \quad (\text{S26f})$$

$$\frac{dK_2(l)}{dl} = \tilde{\Delta}_2^2(l) + \frac{1}{2} [1 - K_2^2(l)] \tilde{\Delta}_c^2(l), \quad (\text{S26g})$$

where the dimensionless coupling constants for the pairing gaps are given in Eqs. (S21), and the dimensionless tunnel amplitude is given by

$$\tilde{t}_n(l) = t_n(l) \sqrt{\frac{a^3(l)}{\hbar^2 u_n^2 \xi_s^2 L}}, \quad (\text{S27})$$

with the hinge length L and the superconducting coherence length ξ_s . The coefficients of the source terms are given by

$$S_n(l) = \frac{m_e v_{F_s}^2 L}{2\pi \Delta_s a(l)} K_0 \left(\frac{\Delta_s a(l)}{\hbar u_n} \right), \quad (\text{S28a})$$

$$S_c(l) = \frac{m_e v_{F_s}^2 L}{2\pi \Delta_s d} e^{-d/\xi_s} |\sin(k_{F_s} d)| \times I_0 \left(\frac{\Delta_s a(l)}{2\hbar \sqrt{u_1 u_2}} \right) K_0 \left(\frac{\Delta_s a(l)}{2\hbar \sqrt{u_1 u_2}} \right), \quad (\text{S28b})$$

with the modified Bessel function of the first- (second-)kind, $I_0(x)$ [$K_0(x)$]. The behavior of Eqs. (S28) is discussed in Ref. [S17], so not repeated here. Rather, we point out that the source terms naturally include the effects of the coherence length and the distance d between the hinges. Namely, due to the factor $e^{-d/\xi_s} |\sin(k_{F_s} d)| \xi_s/d$, the strength of the crossed Andreev pairing is reduced when the distance d increases [S9]. In contrast, in the effective Hamiltonian model, such a dependence is not explicitly included, and has to be incorporated by setting an initial ratio $\Delta_c(0)/\Delta_1(0) < 1$. Nonetheless, as demonstrated below, our numerical calculation show that such a reduction is modest for a small ratio of d/ξ_s , so that the crossed Andreev pairing can eventually dominate over the local pairing in the presence of interactions.

The RG flow equations in Eqs. (S26) are numerically solved

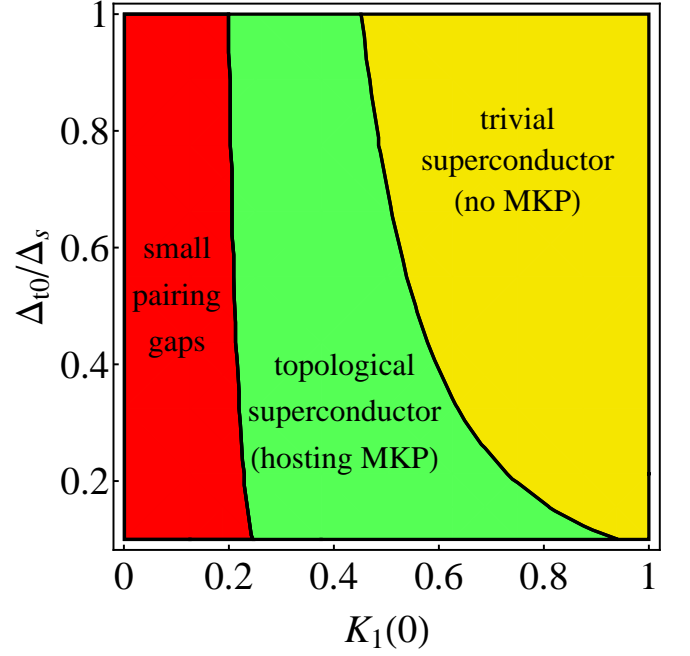


FIG. S2. A phase diagram obtained from the source-term approach, by solving the RG flow equations in Eqs. (S26). Here we define $\Delta_{t0} \equiv \tilde{t}_1^2(0)S_1(0)\hbar u_1/a(0)$, and take the following parameters: $u_1 = u_2 = 10^5$ m/s, $a(0) = 5$ nm, $L = 1$ μ m, $\Delta_s = 0.35$ meV, $k_{F_s} = 10^{10}$ m $^{-1}$, and $d = 50$ nm. As in Fig. 4 in the main text, the green (yellow) region specifies the phase with (without) a Majorana Kramers pair. In the red region, the renormalized values of both $\tilde{\Delta}_c$ and $\tilde{\Delta}_1$ are less than 0.1.

for the following initial parameter values

$$\tilde{t}_1(0) \equiv \tilde{t}_1(l=0) = \tilde{t}_2(l=0), \quad (\text{S29a})$$

$$K_1(0) \equiv K_1(l=0) = K_2(l=0), \quad (\text{S29b})$$

$$S_1(0) \equiv S_1(l=0) = S_2(l=0), \quad (\text{S29c})$$

$$S_c(0) \equiv S_c(l=0), \quad (\text{S29d})$$

$$\tilde{\Delta}_1(l=0) = \tilde{\Delta}_2(l=0) = 0, \quad (\text{S29e})$$

$$\tilde{\Delta}_c(0) = \tilde{\Delta}_c(l=0) = 0. \quad (\text{S29f})$$

This means that the initial values of the pairing gaps are set to zero. Under the RG flow, the pairing gaps are induced by the source terms arising from the tunnel Hamiltonian [see Eq. (S23)]. We obtain the phase diagram by solving Eqs. (S26) with the initial parameters [see Eqs. (S29)] in the regime $K_1(0) \in [0, 1]$ and $\Delta_{t0}/\Delta_s \in [0.1, 1]$, as displayed in Fig. S2. The result is qualitatively similar to the one obtained from the effective Hamiltonian method. Crucially, the result demonstrates that, when the distance between the hinges is $d = 50$ nm, the Majorana Kramers pair is stabilized in a wide region of the parameter space. In addition, we checked the phase diagrams for $d = 100$ nm and 200 nm (not shown), and found no qualitative differences among these values of d . Quantitatively, the green region where the Majorana Kramers pair is present becomes smaller for a larger separation d , as expected.

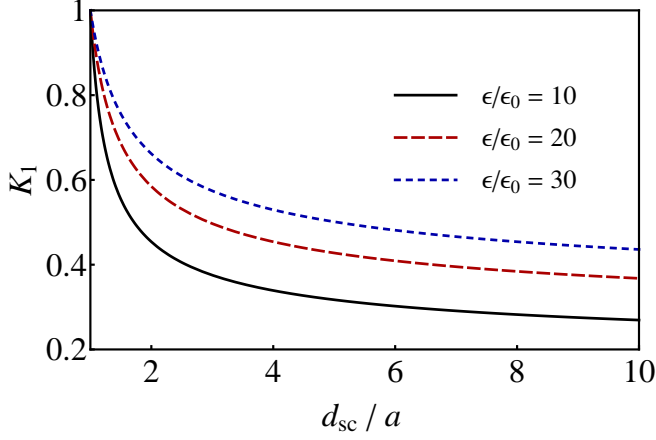


FIG. S3. Interaction parameter (K_1) as a function of the ratio of the screening length to the hinge-state transverse decay length (d_{sc}/a). The legend denotes various values of the relative permittivity, which is the ratio of dielectric constant (ϵ) to its value in vacuum (ϵ_0). The interaction parameter is computed using Eq. (S30) with the parameter $v_F = 10^5$ m/s.

As a side remark, in the small $K_1(0)$ (strongly interacting) regime, the gaps do not flow to exact zero. This is due to the source terms contained in Eqs. (S26). As mentioned above, in contrast to Eqs. (S20), these source terms contribute to the flow equations for $\tilde{\Delta}_n$ and $\tilde{\Delta}_c$ in Eqs. (S26). Therefore, in the presence of a strong interaction, the RG flows of these parameters are stopped by the hinge length of $O(\mu\text{m})$ before going to zero, leading to tiny but finite gaps. In plotting Fig. S2, we therefore label the region in which both the renormalized gaps $\tilde{\Delta}_c$ and $\tilde{\Delta}_1$ are less than 0.1 as the “small pairing gaps” region (marked in red color). This region then corresponds to the normal phase (no pairing) in Fig. 4. In conclusion, the source-term approach confirms the results presented in Fig. 4 in the main text.

VI. Feasibility of the proposed scheme

In this Section we examine the feasibility of our proposal. Taking the first experimentally confirmed material of higher-order topological insulators–bismuth (111) nanostructures [S1]—as an example, we estimate the initial values of the RG parameters for the effective Hamiltonian method presented in the main text, including the interaction parameter K_1 and the bare gap ratio $\Delta_1(0)/\Delta_c(0)$. Then, we discuss suitable materials for the superconductor used for the proximity effect.

We first estimate the interaction parameter K_1 by modifying the formula for the helical edge states of two-dimensional topological insulators [S19]

$$K_1 = \left[1 + \frac{2e^2}{\pi^2 \epsilon \hbar v_F} \ln \left(\frac{d_{sc}}{a} \right) \right]^{-1/2}, \quad (\text{S30})$$

with the Fermi velocity v_F and the transverse decay length

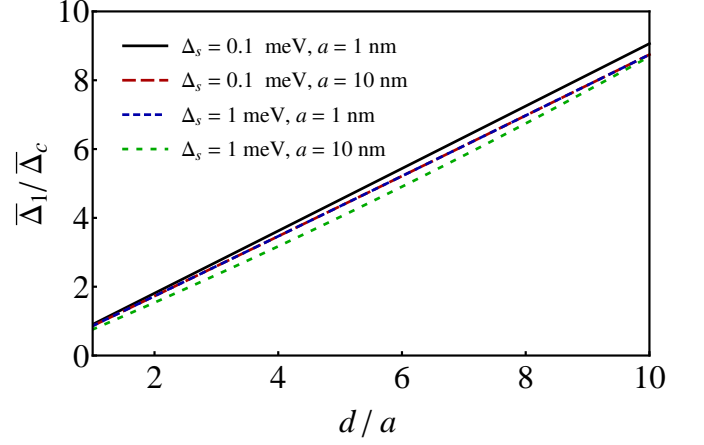


FIG. S4. Bare gap ratio ($\bar{\Delta}_1/\bar{\Delta}_c$) as a function of the ratio of the inter-hinge separation to the decay length (d/a). The legend lists various values of the superconducting gap (Δ_s) and the hinge-state transverse decay length (a). The bare gap ratio is estimated using Eq. (S31) with $\xi_s = \hbar v_{Fs}/\Delta_s$. The adopted values of the other parameters are $v_F = 10^5$ m/s and $v_{Fs} = 10^6$ m/s, which gives the value $\xi_s = 1.9 \mu\text{m}$ for $\Delta_s = 0.35$ meV.

a of the hinge states. In the above, ϵ is the dielectric constant of the material, and d_{sc} is the screening length. We take $v_F = 10^5$ m/s using the relation $\Delta = \hbar v_F/a$, where the finite-size-induced gap $\Delta \sim O(0.1 \text{ eV})$ is obtained from bandstructure calculations for Bi(111) bilayer films [S20, S21], and the transverse decay length $a \sim 1 \text{ nm}$ is extracted from the current-phase relation in asymmetric SQUID experiment [S1]. Even though Bi bulk is a semimetal, we are interested in a Bi nanowire gapped by the finite-size effect. To estimate its dielectric constant, we take several values typical for semiconductors. The screening length d_{sc} depends on the experimental conditions, so we take it as a variable in the range $d_{sc}/a \in [1, 10]$ (we note that a larger d_{sc} will make the interaction parameter even smaller).

The estimated value of the interaction parameter is plotted in Fig. S3, which shows that the estimated K_1 value is typically below 0.6. We remark that the extracted value of $a \sim 1 \text{ nm}$ [S1] indicates quite narrow one-dimensional conducting channels along the hinges. Concluding, the estimated value of the interaction parameter K_1 indicates rather strong electron-electron interactions in the hinge states due to the strong spatial confinements.

Next, we estimate the bare gap ratio using the initial values of the source terms in Eqs. (S28), which generate the pairing gaps under the RG flow and therefore give the initial values of the gaps. Upon approximating the fast oscillating factor $|\sin(k_{Fs}d)| \approx 1$ and the velocities $u_1 \approx u_2 \approx v_F$, we get

$$\frac{\bar{\Delta}_1}{\bar{\Delta}_c} \approx \frac{d}{a} \frac{e^{d/\xi_s} K_0 \left(\frac{\Delta_s a}{\hbar v_F} \right)}{K_0 \left(\frac{\Delta_s a}{2\hbar v_F} \right) I_0 \left(\frac{\Delta_s a}{2\hbar v_F} \right)}, \quad (\text{S31})$$

which depends crucially on the ratio d/a of the inter-hinge separation to the transverse decay length $a = a(0)$. To avoid

possible confusion, in the left-hand side of Eq. (S31), we use the overbar notations $\overline{\Delta}_1$ and $\overline{\Delta}_c$ to refer to the initial values for the effective Hamiltonian method presented in Sec. IV. In the right-hand side, on the other hand, we keep the same notations used for the source-term approach in Eqs. (S28) given in Sec. V. For relevant parameters, we have $d/\xi_s \ll 1$ so that the bare gap ratio grows approximately linearly with the ratio d/a . In Fig. S4, we therefore plot the bare gap ratio as a function of d/a for various Δ_s and a values. On top of the approximately linear dependence on d/a , the bare gap ratio depends weakly on the pairing gap of the parent superconductor Δ_s and the decay length a . Importantly, in the relevant ranges of the parameters $\Delta_s \in [0.1 \text{ meV}, 1 \text{ meV}]$ and $a \in [1 \text{ nm}, 10 \text{ nm}]$, the typical value of $\overline{\Delta}_1/\overline{\Delta}_c$ (i.e. the initial values $\Delta_1(0)/\Delta_c(0)$ for the effective Hamiltonian method) is in the order of unity, which is compatible with the parameters adopted in our RG analysis.

Finally, we comment on suitable materials for the parent superconductor used for the proximity effect. The phase diagram predicted with the source-term approach (see Fig. S2) indicates that Majorana Kramers pairs can be achieved using higher-order topological insulators with the inter-hinge separation $d \sim O(10\text{--}100 \text{ nm})$ in the proximity of a superconductor with the gap $\Delta_s \sim O(0.1 \text{ meV})$ and the coherence length $\xi_s \sim O(1 \mu\text{m})$. These material parameters suggest that aluminum is a suitable material for the parent superconductor (due to its long coherence length). We remark that the observed ballistic supercurrent with nearly perfect transmission indicates good contacts between the hinge states and a superconductor [S1, S22], suggesting that bismuth nanowires offer a suitable platform for proximity-induced superconductivity.

In summary, together with the phase diagram presented in the main text (see Fig. 4), we conclude that Bi nanowires in the proximity of an aluminum superconductor offer a suitable platform for stabilizing Majorana Kramers pairs. We stress that the proposed scheme can be implemented in other higher-order topological insulators hosting helical hinge states, and is not restricted to the specific material. We hope that this work can stimulate studies searching for other promising materials for realization of Majorana Kramers pairs. Given the recent rapid progress on the hunting of topological materials [S23], we are optimistic that our proposal can be realized in the near future.

-
- [S1] F. Schindler, Z. Wang, M. G. Vergniory, A. M. Cook, A. Murani, S. Sengupta, A. Y. Kasumov, R. Deblock, S. Jeon, I. Drozdov, H. Bouchiat, S. Guéron, A. Yazdani, B. A. Bernevig, and T. Neupert, *Nat. Phys.* (2018), 10.1038/s41567-018-0224-7.
 - [S2] L. Fu and C. L. Kane, *Phys. Rev. Lett.* **100**, 096407 (2008).
 - [S3] C. L. M. Wong and K. T. Law, *Phys. Rev. B* **86**, 184516 (2012).
 - [S4] A. Keselman, L. Fu, A. Stern, and E. Berg, *Phys. Rev. Lett.* **111**, 116402 (2013).
 - [S5] F. Zhang, C. L. Kane, and E. J. Mele, *Phys. Rev. Lett.* **111**, 056402 (2013).
 - [S6] A. Haim, A. Keselman, E. Berg, and Y. Oreg, *Phys. Rev. B* **89**, 220504 (2014).
 - [S7] C. Schrade, A. A. Zyuzin, J. Klinovaja, and D. Loss, *Phys. Rev. Lett.* **115**, 237001 (2015).
 - [S8] S. Hoffman, J. Klinovaja, and D. Loss, *Phys. Rev. B* **93**, 165418 (2016).
 - [S9] C. Reeg, J. Klinovaja, and D. Loss, *Phys. Rev. B* **96**, 081301 (2017).
 - [S10] C. Schrade, M. Thakurathi, C. Reeg, S. Hoffman, J. Klinovaja, and D. Loss, *Phys. Rev. B* **96**, 035306 (2017).
 - [S11] J. Klinovaja, A. Yacoby, and D. Loss, *Phys. Rev. B* **90**, 155447 (2014).
 - [S12] J. Klinovaja and D. Loss, *Phys. Rev. B* **92**, 121410 (2015).
 - [S13] T. L. Schmidt, S. Rachel, F. von Oppen, and L. I. Glazman, *Phys. Rev. Lett.* **108**, 156402 (2012).
 - [S14] C.-H. Hsu, P. Stano, J. Klinovaja, and D. Loss, *Phys. Rev. B* **96**, 081405 (2017).
 - [S15] C.-H. Hsu, P. Stano, J. Klinovaja, and D. Loss, *Phys. Rev. B* **97**, 125432 (2018).
 - [S16] T. Giamarchi, *Quantum Physics in One Dimension* (Oxford University Press, New York, 2003).
 - [S17] M. Thakurathi, P. Simon, I. Mandal, J. Klinovaja, and D. Loss, *Phys. Rev. B* **97**, 045415 (2018).
 - [S18] P. Virtanen and P. Recher, *Phys. Rev. B* **85**, 035310 (2012).
 - [S19] J. Maciejko, C. Liu, Y. Oreg, X.-L. Qi, C. Wu, and S.-C. Zhang, *Phys. Rev. Lett.* **102**, 256803 (2009).
 - [S20] Y. M. Koroteev, G. Bihlmayer, E. V. Chulkov, and S. Blügel, *Phys. Rev. B* **77**, 045428 (2008).
 - [S21] M. Wada, S. Murakami, F. Freimuth, and G. Bihlmayer, *Phys. Rev. B* **83**, 121310 (2011).
 - [S22] A. Murani, A. Kasumov, S. Sengupta, Y. A. Kasumov, V. T. Volkov, I. I. Khodos, F. Brisset, R. Delagrèze, A. Chepelianskii, R. Deblock, H. Bouchiat, and S. Guéron, *Nat. Commun.* **8**, 15941 (2017).
 - [S23] M. G. Vergniory, L. Elcoro, C. Felser, B. A. Bernevig, and Z. Wang, *ArXiv e-prints* (2018), arXiv:1807.10271 [cond-mat.mtrl-sci]